

Au@Pt Hybrid Nanorods Encapsulated in B, S dual-doped Graphene as Highly Sensitive Immunosensing Platform for Electrochemical Determination of Aflatoxin B₁

Xianlan Chen^{1,2}, Huajian Li³, Guowei Zhang^{1,2}, Shaoping Feng^{1,2,*}, Guangming Yang^{1,2,*}, Ling Shi^{1,2}, Wei Liu^{1,2,*}, Guiyang, Liu^{1,2} and Haibo Pan⁴

¹ School of Science, Honghe University, Mengzi, 661199, Yunnan, China;

² Key Laboratory of Natural Pharmaceutical & Chemical Biology of Yunnan Province, Mengzi, 661199, Yunnan, China

³ College of Food Science and Technology, Yunnan Agricultural University, Kunming, China

⁴ Fujian Key Lab of Medical Instrument & Pharmaceutical Technology, Yishan Campus, Fuzhou University, Fuzhou, Fujian, 350002, China

*E-mail: shaopingfeng@126.com; 13489086418@163.com; yangguangmingbs@126.com; liuwei4728@126.com

Received: 13 February 2020 / Accepted: 9 April 2020 / Published: 10 June 2020

A specific electrochemical immunosensor for ultra-sensitive determination of Aflatoxin B₁ (AFB₁) was developed according to a dual enhancing strategy. The dual-doped graphene (BS-G) was obtained by a simple microwave-assisted hydrothermal approach, sulfur and boron affinity for peanut-shaped Au@Pt NRs embedded into BS-G nanosheets, ultrathin BS-G effectively enwrapped most of the individual Au@Pt NRs with excellent dispersibility. It is noteworthy that two faces at the interface between (002) crystal faces of BS-G and (111) planes of Au@Pt NRs are compatible, accelerating the charge transfer between the hybrid nanocatalysts and AFB₁. Moreover, the highly dispersed COOH groups and defect sites of the BS-G precisely control the orientation of anti-AFB₁ immobilized on the sensor surface, meanwhile, the strong electronic interactions endow the Au@Pt NRs/BS-G hybrid nanocatalysts with remarkable biocompatibility and multivalent affinity interactions with the high molar ratio of anti-AFB₁ for enhanced immunoreactions. Thus, the designed immunosensor exhibits ultra-efficient electron-transfer abilities, excellent sensitivity, and favorable selectivity, the detection limit is 0.0052 ng·mL⁻¹ and the linear range is 0.025-60.00 ng·mL⁻¹.

Keywords: AFB₁; B, S dual-doped grapheme; Au@Pt NRs; Au@Pt NRs/BS-G hybrid nanocatalysts, Electrochemical immunosensor

1. INTRODUCTION

Contamination of food by mycotoxins is one of the most actual problems because the toxins threaten human and animal health, and consequently on economic aspects related to food commerce

and food waste [1, 2]. Aflatoxin B₁ (AFB₁) is the major mycotoxin that produced mainly by *Aspergillus flavus* and *A. parasiticus* and found to be colonizing with crops [3, 4]. There has sufficient evidence of carcinogenicity and teratogenicity of AFB₁ through the food chain and accumulate in the human body [5]. Traditional methods for the determination of AFB₁ possess high sensitivity and reliability but require high costs, laborious processes and long analysis time, such as thin-layer chromatography [6], liquid chromatography-mass spectrometry [7] and enzyme-linked immunosorbent assay [8]. Fortunately, electrochemical immunosensor is a reliable alternative analysis technique owing to the features of rapid detection, high-sensitivity, and compact instrumentation [9, 10]. However, many immunosensors which constructed based on antibodies or enzyme working electrodes were suffered from low conductivity and active electrode surface area [11].

Optimized designing of highly active electrode catalyst as a signal amplifier was considered as a crucial point to the design of high-performance immunosensing [10, 12]. The novel nanomaterials with numerous remarkable properties have been demonstrated can notably improve the performance of electrochemical immunosensor [13, 14]. Gold nanomaterials-based immunosensor have attracted unique interest in the bioanalytical field, especially, gold nanorods (Au NRs) would be a potential candidate for signal transduction and amplification due to well-developed methodology of covalent binding of biomolecules on the surface of Au NRs. Meanwhile, Au NRs have superior physical and chemical properties such as easy fabrication, high surface-to-volume ratio, good biocompatibility and unique catalytic activity, which are even more attractive for the design of immunosensor [15, 16]. However, the surfactant has been widely in the synthesis of Au NRs, the Au NRs have been tightly encapsulated by stabilizing ligands or surfactant, lacking antigen-targeting and antibodies-loading capability, even which displayed significant toxicity [17]. As a result, controlled surface modification of Au NRs to eliminate or reduce the adverse effect of cetyltrimethylammonium bromide (CTAB) is of critical importance [18]. Fortunately, modify of Pt nanodots on the surface of Au NRs can effectively reduce the adverse effect of CTAB. It is suggested that the formation of the Pt shell on the surface of Au NRs provides a novel approach to construct immunosensor due to the antioxidant potential and minimal toxicity in vivo of Pt nanodots [19]. Moreover, Y. Lu had employed the core-shell Au-Pt microgels with controlled morphology and excellent stability as “smart nanoreactors” for the catalytic active bimetallic nanoparticles [20]. In this paper, core-shell bimetallic Au@Pt nanorods (Au@Pt NRs) were obtained by Au NRs serve as the core, modification of Pt nanodots on the surface of Au NRs via wet chemical reduction method. This core-shell hybrid nanostructure indicating excellent conductivity, pure contact surface and good biocompatibility can provide an extremely platforms for the adhesion of monoclonal anti-aflatoxin B₁ (anti-AFB₁) antibodies because of their anisotropic shape and simple surface functionalization. More interestingly, the Au@Pt NRs with excellent electrocatalytic activity and higher stability are even more attractive for the design of immunosensor.

Another efficient strategy is to disperse Au@Pt NRs onto a suitable support with high surface area and excellent electrical conductivity, the possible reasons being that the Au@Pt NRs are vulnerable to changes in size, shape and interface conditions when they are long-term or recycle catalyze [21]. The specific structures of a single layer of sp²-hybridized carbon atoms of graphene can provide a platform for Au@Pt NRs to design composite nanomaterials [22]. Nevertheless, graphene nanosheets had strong tendency of agglomeration, perfect graphitization and low defect level, which is

difficult to uniformly anchor Au@Pt NRs [23], thus significantly decrease the contact between the active materials and electrolyte. The most gratifying discovery is that the heteroatom doping (e.g., N, P, B, S, or I) can tailor the interaction between graphene and metal catalyst [24, 25]. M. Shumba et al. have demonstrated that doping graphene with multiple functionalities such as N, S can create plenty of defect sites in the edges of graphene sheets and basal planes, which can employ as loading sites for anchoring gold nanorods, the interaction of gold nanorods with sulfur through Au-S bonds [26]. Specifically, strong coupling between gold nanorods and graphene with local electric fields and charge transfer has been proved [27]. In addition, the high-lying B-C bonding orbitals of B-doping graphene probably facilitated the formation of strong σ bonds between Pt atom and the graphene sheet [28], and the doping of B atoms can increase the electron density of Pt and reduce the d-band center of Pt, which result in the decreasing of C-H bond energy of target molecules [23]. In particular, the heteroatoms doping can regulate the band structure of graphene and form a band gap between the valence and conduction bands, thus endow graphene with excellent conductivity, long-term stability and structural properties for enhancement of the electrocatalytic activity [29]. The dual-doped graphene can introduce the electrochemically active sites compare with the single doped graphene, showing significantly improved electrochemical sensing performances [30].

Most recently, various well-known strategies have been reported for producing dual-doped graphene, such as laser irradiation [31], chemical vapor deposition [32], ultrasonic-assisted synthesis [33], plasma treatment [34], thermal treatment [35] and hydrothermal synthesis [36]. Compared with above-mentioned methods, the interaction between microwave-assisted hydrothermal approach and high frequency electromagnetic radiation will result in a much faster reaction, low-cost, environmentally friendly, significant energy-saving and time-saving [37, 38]. Moreover, this method is capable of synthesizing B,S dual-doped graphene produce plenty of defect sites and COOH groups in the edges of graphene sheets and basal planes, which not only highly offered the capability of targeting for antigen-antibody but also enhance effectively the sensitivity of an immunosensor.

In this work, an effective and simple method is investigated to fabricate B,S dual-doped graphene (BS-G) with unique three dimension porous frameworks via microwave-assisted hydrothermal approach. Sulfur and boron affinity for Au@Pt NRs encapsulated in BS-G nanosheets, forming Au@Pt NRs/BS-G hybrid nanocatalysts. The encapsulation of BS-G not only eliminated the cytotoxicity of relatively small amounts of CTAB but also provided anchor points to Au@Pt NRs for further modification. Most interesting is the highly dispersed COOH groups on the BS-G will precisely control the orientation of anti-AFB₁ antibody immobilized on the sensor surface, which will result in an excellent adsorption of AFB₁. After that, the Au@Pt NRs/BS-G hybrid nanocatalysts as a multi-component matrix have been used for preparation of BSA/anti-AFB₁/Au@Pt NRs/BS-G/GCE for determination of AFB₁. The bioelectrode with excellent sensitivity and ultralow detection limit for AFB₁ has been designed in this study.

2. EXPERIMENTAL

2.1 Reagents

Aflatoxin B₁ (AFB₁), HAuCl₄·3H₂O, H₂PtCl₆, monoclonal anti-AFB₁ antibody (anti-AFB₁),

albumin form bovine serum (BSA \geq 98%) were obtained from Sinopharm Chemical Reagent Co. Ltd. Graphite (99.95%, 325 mesh) powder, silver nitrate (AgNO₃), NaBH₄, CTAB, L-ascorbic acid (AA), Na₂S and Boron trioxide powder (B₂O₃, 99%) were from Alfa Aesar. NaH₂PO₄-Na₂HPO₄ (0.1 M) mixed solution was used as phosphate buffer solution (PBS) to adjust the pH. All other chemicals used were of AR grade and used without further purification.

2.2 Instruments and characterizations

UV-vis spectra (Perkin-Elmer Lambda 900 USA) was used to obtain UV-vis absorption spectra of Au seed, Au NRs and Au@Pt NRs. XRD (X'pert, Philips, Holland) and XPS (Thermal Scientific K-Alpha XPS spectrometer) were employed to investigate the crystalline structures and elemental compositions of Au NRs, Au@Pt NR and BS-G. The characteristics of the Au NRs and Au@Pt NRs were determined using energy-disperse X-ray spectra (EDS). SEM (Nova Nano SEM 230, FEI, USA), Nano-beam electron diffraction (NBED) and HRTEM (Tecnai G2 F20 S-TWIN, 200 kV, FEI Company, USA) were obtained to understand the surface morphologies and microstructure of the synthesized materials.

The electrochemical workstation (CHI 660C, Shanghai) was used to record cyclic voltammogram (CV) and differential pulse voltammogram (DPV). The electrochemical cell consisted of a three electrode system with a bare gold electrode (GE, 3.0 mm in diameter) or modified working electrode as a working electrode, a platinum wire as a counter electrode and Ag/AgCl electrode as a reference electrode. EIS (Autolab 302N, Metrohm China Co. Ltd., Switzerland) measurements were performed in 10.00 mM [Fe(CN)₆]^{3-/4-} containing 0.10 M KCl. The amplitude of ac voltage was \pm 5.0 mV and the frequency was in the range of 10⁵ to 0.1 Hz. Before measurements, the mixed solution (0.10 M PBS, 10.00 mM [Fe(CN)₆]^{3-/4-} and 0.10 M KCl) was added into the electrochemical cell after purging with N₂ for 15 min.

2.3. Preparation of Au@Pt NRs

The Schematic diagram of forming the Au@Pt NRs hybrid nanocatalysts was shown in Scheme 1AII. Specially, the synthesis procedure of Au@Pt NRs consists of three steps.

The first step was for the synthesis of Au seeds. Briefly, 5.0 mL CTAB (0.20 M) and 5.0 mL of HAuCl₄ (0.50 mM) were added to a beaker to prepare a seed solution. Then, 0.6 mL 0.01 M NaBH₄ solution which was freshly prepared and ice-cold was quickly added immediately and stirred for 2.0 min. The color of the mixture solution changed from dark yellow to brownish, implying the formation of the Au seeds solution. Finally, the seed solution was aged for 2.0 h at 25 °C

The second step was for synthesis of Au NRs via modified seed-mediated growth [39], 5.0 mL 0.20 M CTAB solution was added to the mixture solution which contained 0.2 mL 4.00 mM AgNO₃ and 5.0 mL of 1.00 mM HAuCl₄ and mixed by gentle shaking. Freshly prepared 0.32 mL of 8.00 mM AA was then added sequentially. After that, 12.0 μ L Au seeds were added under vigorous stirring and then the reaction flask was transferred to the water-bath. For all the reactions, the water-bath was

coated by the cover to avoid the light and the reaction flask left undisturbed overnight for longitudinal overgrowth. Finally, the as-prepared Au NRs were washed and centrifuged three times to remove all dissociative CTAB. The resulting Au NRs were redispersed in ultra-pure water (10.0 mL) and used for preparation of Au@Pt NRs.

The third step was for the seeded synthesis of Au@Pt NRs, 6.0 mL the above Au NRs was placed in a beaker contained 225.0 μL of 20.0 mM H_2PtCl_6 and 9.0 mL of ultra-pure water. The mixture solution were placed in an ice bath (4.0 $^\circ\text{C}$) and dispersed uniformly through stirred for 10.0 min. Finally, a freshly prepared 3.0 mL 0.10 M AA was added gradually into the solution under stirring and stirred for another 40.0 min. The color of this mixture solution changed from deep purple to black, these observations suggest that the bimetallic Au@Pt NRs were formed.

2.4. Preparation of BS dual-doped graphene and Au@Pt NRs/BS-G hybrid nanocatalysts

The crucial factor for constructing an immunosensor successfully was stably immobilized antibodies or antigens on the nanomaterial signal amplifier with excellent biological recognition properties [14]. The preparation of BS-G via hydrothermal approach could introduce highly dispersed COOH groups on the surface (Scheme 1AI), which will intensively adsorb immobilization of anti-AFB₁, opening a way to modify a new signal amplifier with high electrocatalytic activity for real immunosensor applications.

The microwave-heating combining with hydrothermal can cause enhanced kinetics of crystallization and promote the generation of new phases. BS-G was prepared by microwave-assisted hydrothermal approach using microwave apparatus. 50.0 mg GO which dissolved in 100.0 mL ultra-pure water was sonicated until uniform dispersion was obtained, followed by the addition B_2O_3 powder and Na_2S which are the source of boron and sulfur were mixed with GO in a mass ratio of 25:5:1. Finally, the mixture was sonicated for 1.0 h and transferred into sealed Teflon autoclaves, which were put in the Microwave Digestion System (MOT-100N, Germany) at 473.0 K for 3.0 h. The resulting black floccus product (BS-G) was washed and centrifuged 4~5 times to remove excess B_2O_3 and Na_2S with alcohol and ultra-pure water, respectively.

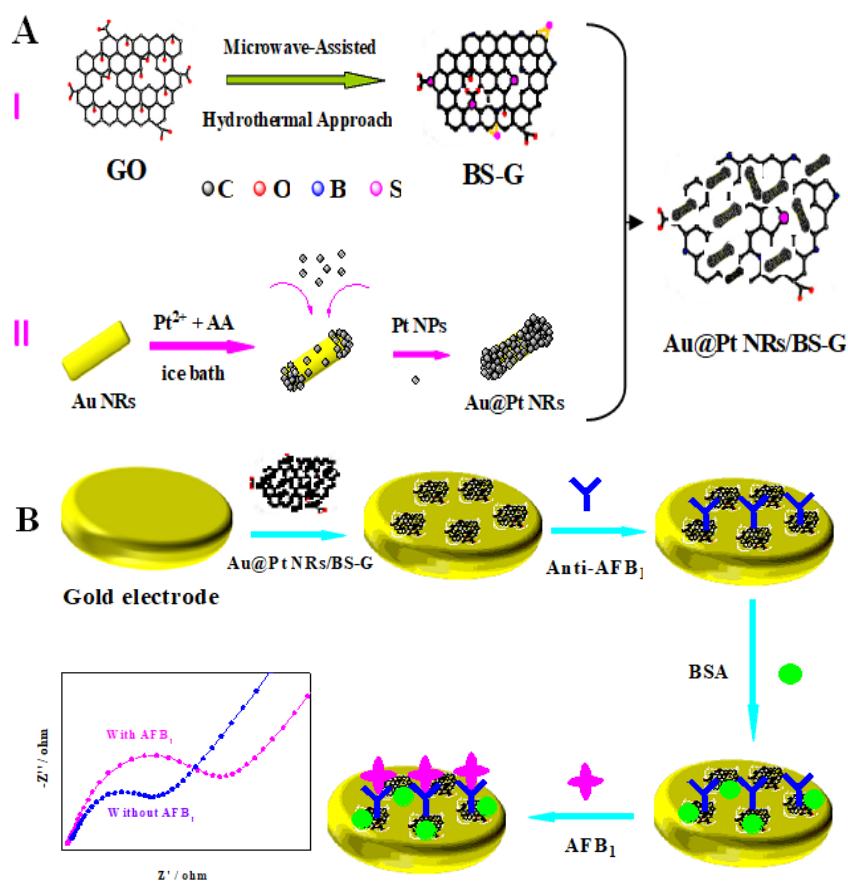
The Au@Pt NRs/BS-G hybrid nanocatalysts were fabricated by adding 15.0 mL Au@Pt NRs to BS-G (2.0 mL) solution with vibration on a vortex mixer for 2 h at 25 $^\circ\text{C}$. During the vibration process, sulfur and boron affinity for Au@Pt NRs embedded in BS-G nanosheets. Moreover, the Au@Pt NRs encapsulated in the nanosheets would result in the increasing of the accessible surface area of BS-G, highly dispersed COOH groups and improved exposure of defect sites in the edges of graphene sheets and basal planes. This nanostructure will become as a perfect signal amplifier, not only be beneficial to immobilize antibodies or antigens for the successful immunosensor construction, but will improve stability and electrocatalytic activity of the Au@Pt NRs/BS-G hybrid nanocatalysts.

2.5. Fabrication of the immunosensor

The bare GE was polished with alumina powders (1.0, 0.3 and 0.05 μm) in series. Afterward,

the electrode was ultrasonicated in nitric acid solution (50%), ethanol and ultra-pure water successively about 5.0 min after each polishing, respectively. Finally, the electrode was dried under pure N₂. Then, the cyclic scanning was tested in 0.50 M H₂SO₄ at -0.3~1.5 V until a voltammogram characteristic of a clean GE was established, and then the electrode was washed with ultra-pure water and dried under pure N₂ before measurement.

After activation, Au@Pt NRs/BS-G hybrid nanocatalysts film-modified gold electrode (Au@Pt NRs/BS-G/GE) was obtained by 7.0 μL of the Au@Pt NRs/BS-G hybrid nanocatalysts were coated on the electrode surface and then evaporated of the solvent at room temperature. Afterward, a volume of 9.0 μL anti-AFB₁ (100.00 μg·mL⁻¹) were pipetted over the reactive part of the modified electrode and incubated at 37.0 °C for 50.0 min, then rinsed with ultra-pure water to remove the unbounded anti-AFB₁ and dried at room temperature, formed structure was indicated as anti-AFB₁/Au@Pt NRs/BS-G/GE. After drying in air of the modified electrode, the non-specific sites of fabricated immunoelectrode was blocked with 10.0 mL BSA (2.0 wt.%) at 37.0 °C for 40.0 min. Ultimately, the immunosensor (BSA/anti-AFB₁/Au@Pt NRs/BS-G/GE) was incubated at 37.0 °C for 50.0 min with 9.0 μL different concentrations of AFB₁ (AFB₁/BSA/anti-AFB₁/Au@Pt NRs/BS-G/GE), followed by washing with PBS for 3-4 times prior to electrochemical measurements. The schematic illustration of the preparation of the electrochemical immunosensor and assay procedure was shown in Scheme 1B.



Scheme 1. (A) Schematic diagram of forming the Au@Pt NRs/BS-G hybrid nanocatalysts, (I) Schematic diagram of the synthesis of BS-G; (II) Model proposed for the formation of Au@Pt NRs. (B) Schematic illustration of the preparation of the electrochemical immunosensor and assay procedure.

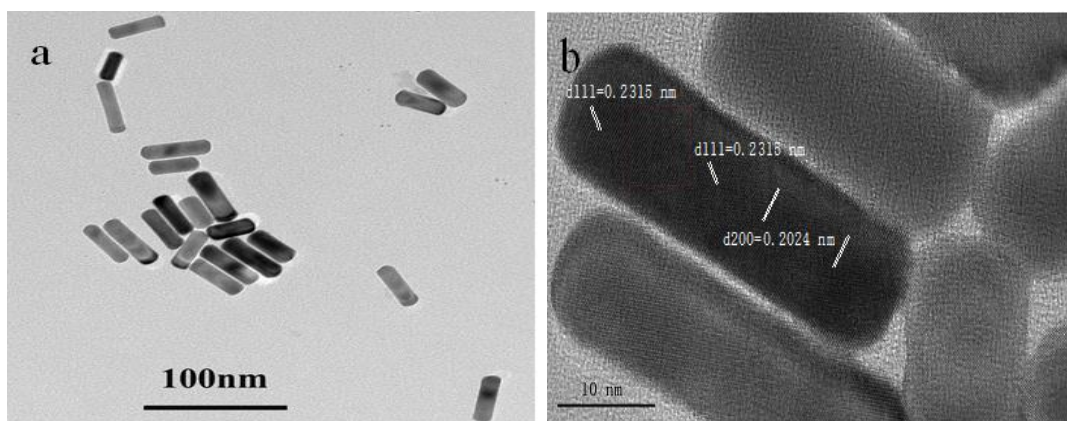
2.6. Sample preparation

The preparation of samples including non-contaminated rice and peanut was as same as in the previous literature [40]. A 1.0 g finely pulverized rice and peanut were spiked with a certain amount of AFB₁ and mixed in high speed vortex, respectively. The samples were extracted with 5.0 mL methanol-water (80:20, v/v) for 45.0 min and then centrifuged at 10000.0 rpm for 15.0 min. The obtained samples were diluted into desired concentration with PBS (pH 7.5) for further testing with the immunosensor and stored at -20.0 °C before using. Next, the AFB₁ spiked rice and peanut were incubated on the sensing surface for 50 min, washed with PBS and dried under N₂ before measurement.

3. RESULTS AND DISCUSSION

3.1. Physicochemical characterization of Au NRs and Au@Pt NRs

The structure of the Au NRs is crucial for forming bimetallic Au@Pt NRs. Therefore, TEM and HRTEM images of the AuNRs were presented in Fig. 1. As was shown in Fig. 1a, there were obvious Au rods in the bright field image, which their average width and length were of ~12.5 nm and ~40.0 nm, respectively. The relatively concentrated aspect ratio (3.5 ± 0.4) distribution with smooth appearance and rounded ends indicates that the size of Au NRs is very homogeneous. In order to observe more clearly, the HRTEM image of Au NRs was obtained (Fig. 1b). Obviously, the Au NRs remain single crystalline with a smooth surface and the lattice fringes were clearly visible, indicating the high quality of the Au NRs. The crystal structure of the Au NRs reveals a single crystal of Au NRs growing along an elongated growth along the [111] direction, and the fringe spacing of (200) was measured to be 0.2024 nm, which also indexed corresponding to FCC gold. Fig. 1c shows the nano-beam electron diffraction (NBED) pattern at the location are marked by white frame in Fig. 1b, the spots correspond to the (313), (200), (113), (113), (113) and (200) reflections of Au with zone axes (ZA) of [031] (JCPDS cards 04-0784) [39]. The EDS results for the locations marked by “white frame area” in Fig. 1b are shown in Fig. 1d, from which the Au NRs only contains Au and Ni which stem from nickel grid.



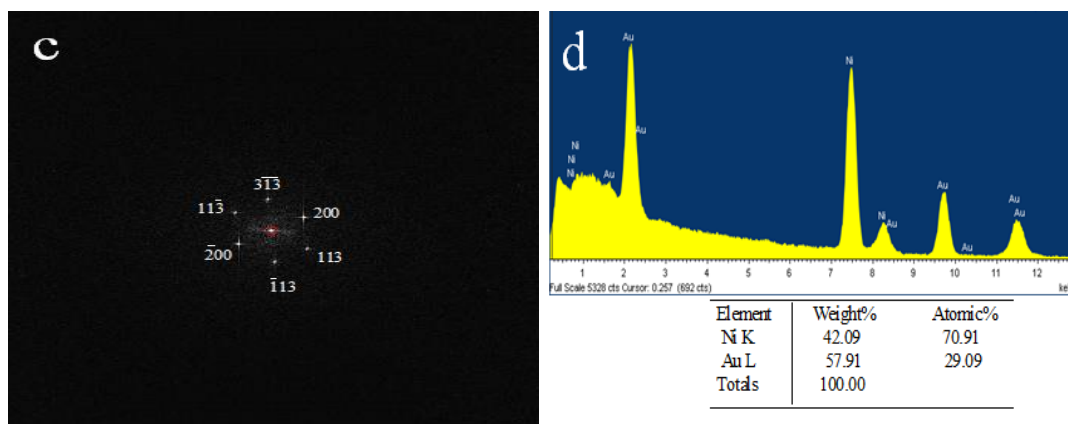


Figure 1. (a) TEM images corresponding to Au NRs. (b) high-magnification TEM (HRTEM) image of the Au NRs. (c) NBED pattern in the location marked by white frame in (b). (d) EDX spectrum of Au NRs (Ni from the nickel grid).

Fig. 2a illustrates the UV-vis spectra of the Au seed, Au NRs and Au@Pt NRs. The absorption band centered at 522.0 nm corresponds to the Au seeds (curve I). As expected, there are two characteristic peaks appearing at 525.0 and 666.0 nm, corresponding to peak positions of transverse and longitudinal surface plasmon resonances (LSPR) of the Au NRs, respectively (curve II). Addition of Pt shell to the Au NRs was found to red-shift the LSPR band to 690.0 nm (curve III), these effects are associated with modification of both the shape and the dielectric characteristics of the nanorod upon Pt deposition.

TEM images revealed that the “peanut” shape of Au@Pt NRs was formed (Fig. 2b), which was attributed to the site-dependence of the CTAB binding strength on the surface of the Au NRs and the deposition of Pt at the ends of the rods [42]. In addition, the most relatively strained (111) bridging facets are preferred locations for Pt deposition, which result in the growth of Pt at the ends of the rods [41]. The corresponding HRTEM image of heterogeneous bimetallic Au@Pt NRs was shown in Fig. 2c, where a clear epitaxial interface between the original Au NRs and the newly grown Pt layer with diameter about 2-4 nm. Moreover, Fig. 2c reveals that a dark core surrounded by a light-color shell in bimetallic Au@Pt NRs. The corresponding fast Fourier transform (FFT) pattern of Fig. 2c further confirmed that the growth direction of Pt was along [100] direction on both sides of the rod (Fig. 2d). The EDS image in Fig. 2e show that the hybrid Au@Pt NRs have thinner Pt shell surround with the core Au NRs, which contained an atomic ratio of 0.11% Pt and 29.11% Au and displayed a further red shift in the LSPR band to longer wavelengths in Fig. 2a (curve III).

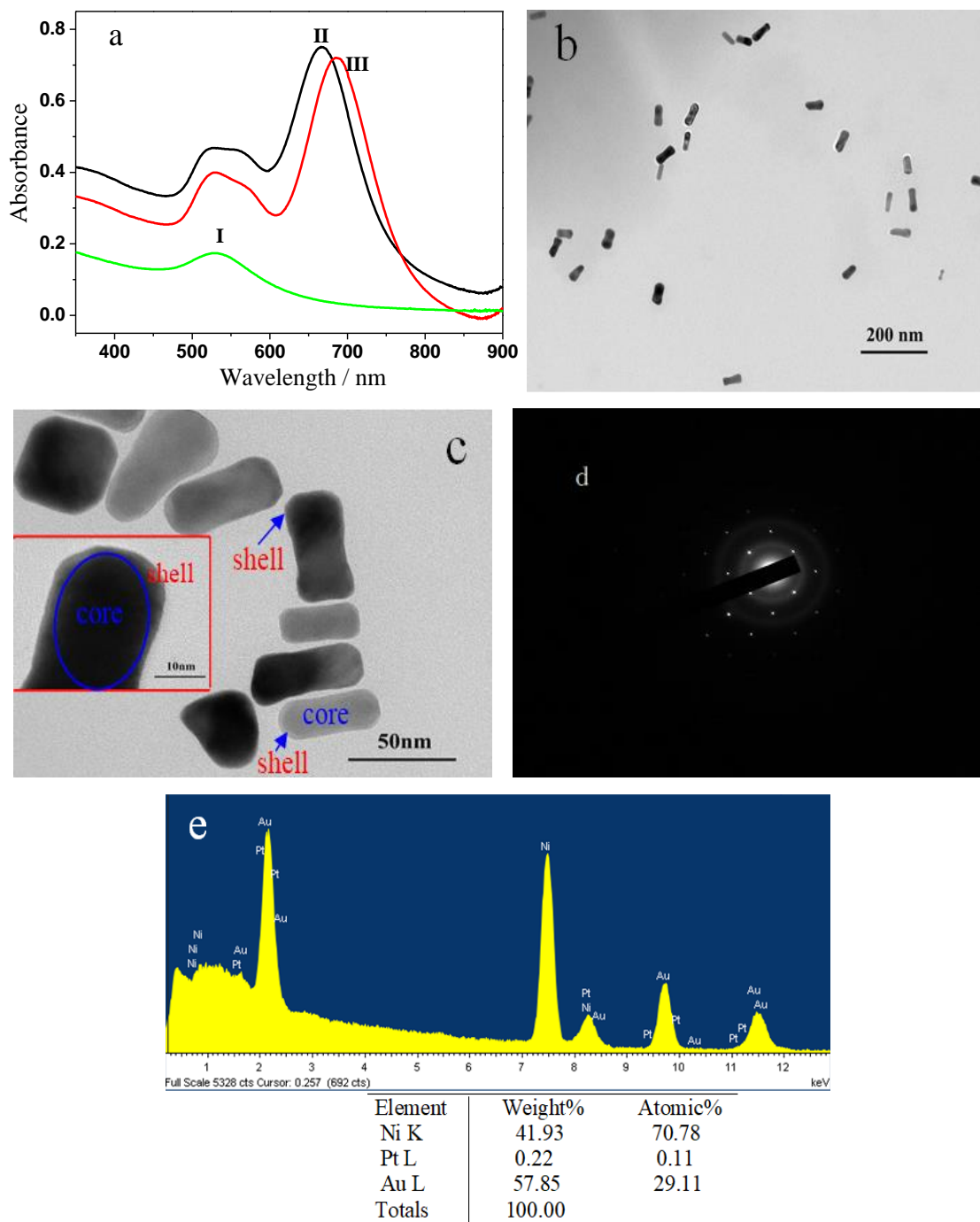


Figure 2. (a) UV-vis absorption spectras of (I) Au seeds, (II) Au NRs before and (III) after deposition of Pt shell. (b) TEM image of peanut-shaped Au@Pt NRs. (c) The corresponding HRTEM image of the Au@Pt NRs. Insert: It shows the Au@Pt NRs with a core and a thin shell. (d) Diffraction patterns of Au@Pt NRs for different directions. (e) EDX analysis for Au@Pt NRs (Ni from the nickel grid).

The comparisons of XRD between Au NRs and Au@Pt NPs were displayed in Fig. 3a. The diffraction angles (2θ) of 38.24 , 44.44 , 65.4 , 77.66 , and 81.80° were responded to the diffraction peaks of (111), (200), (220) and (311) crystal faces of Au, respectively. The similar peaks are obtained

between Au@Pt NRs and Au NRs, all the peaks can be responded to face-centered cubic Au and Pt belonging to Fm3m space group (JCPDS file No. 04-0784, 04-0802). It is observed that the diffraction angles are changed from 38.24 to 38.22° by analyzing the (111) facet of FCC corresponding to the strongest peak position, and the patterns of Pt were overlapped with Au. Moreover, it is worth noticing that the diffraction angle (2θ) of (200), (220), (311), and (222) facets of Au@Pt NRs move right 0.02, 0.06, 0.02 and 0.02° compare with Au NRs, respectively. The reason is the discrepancy of atom weight and the electron density between Au and Pt, indicating that the Au@Pt NRs were ordered structures with good crystallization.

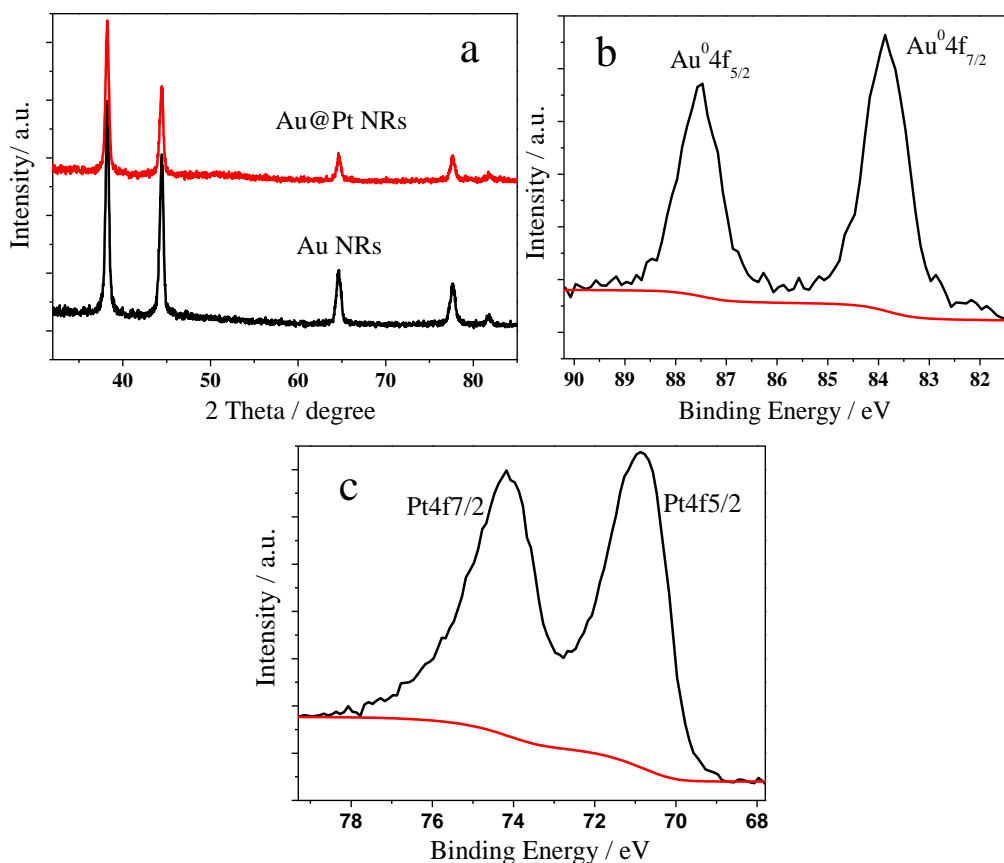


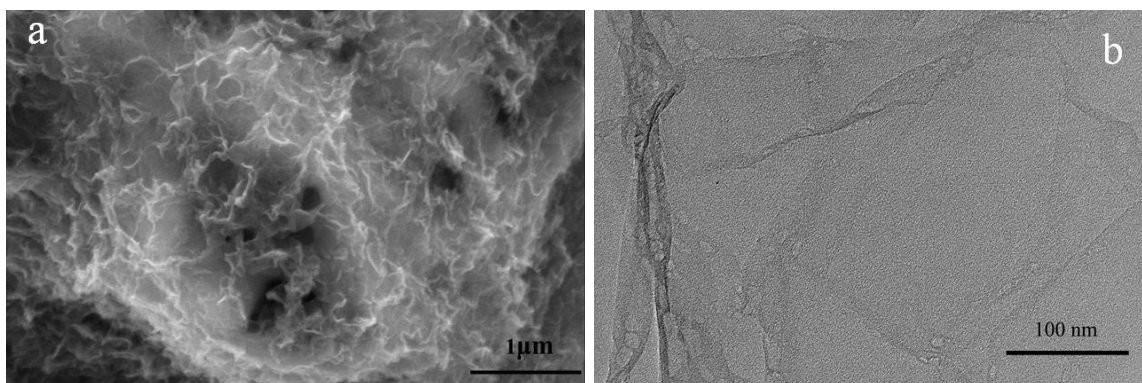
Figure 3. (a) XRD patterns of Au NRs and Au@Pt NRs. (b) High resolution XPS spectra of the Au 4f in Au@Pt NRs. (c) XPS spectra of the Pt4f in the Au@Pt NRs.

Besides, XPS Au@Pt NRs were investigated to obtain the elemental compositions and the results were shown in Fig. 3b,c. An Au4f signal (metallic Au) and a Pt4f signal (metallic Pt) were observed in XPS patterns of the Au@Pt NRs, which was shown in Fig. 3b and Fig. 3c, respectively. Compared with the standard data of Au⁰ (4f_{7/2} = 83.77 eV and 4f_{5/2} = 87.70 eV), the binding energies of Au 4f_{7/2} are shifted to higher value (4f_{7/2} = 83.87 eV) and Au 4f_{5/2} are shifted to lower value (4f_{5/2} = 87.47 eV). Analogously, the binding energies of Pt4f (4f_{7/2} = 70.87 eV, 4f_{5/2} = 74.17 eV) shifts negatively by 0.07 and 0.08 eV compared to Pt⁰ (70.94 and 74.25 eV for Pt4f_{7/2} and Pt4f_{5/2}, respectively), implying the higher electron density of Pt, which would be attributed to the low electronegativity of the electron transfer from Au to Pt.

3.2. Physicochemical characterization of BS-G and Au@Pt NRs/BS-G hybrid nanocatalysts

The morphology and microstructure of the as-prepared BS-G was investigated by SEM and TEM. An interconnected sheet-like of graphene nanosheets with folded structure can be discerned in SEM image (Fig. 4a), the highly folded structure due to a large curvature formed on the graphene surface by the substitution and doping between carbon and larger-sized S heteroatoms. It can be clearly seen that BS-G (Fig. 4b) still maintains paper-like structures with relatively high electron transparency, where the surface is covered with wrinkles and corrugations. This suggests that B and S heteroatoms doping does not change the crumpled-like surface and three dimension structure of the original graphene with the residual functional groups, which will contribute to the facile access of analyte and efficient transfer of electrons. From the HRTEM image of BS-G in Fig. 4c, few-layered graphene sheets with well-defined interplanar spacing of 0.395 nm corresponding to (002) plane of graphene can be identified, much larger than 0.335 nm of graphite crystal structure [43]. More interesting is doping sulfur and boron atoms produce a large number of nanoditchs in locally ordered structure is clearly observed in an augmentation of BS-G, followed by these defect sites (such as vacancies and edge sites) in the basal planes will be improve the interfacial properties of Au@Pt NRs and integrate the advantages of anti-AFB₁ and AFB₁.

The elemental contents of BS-G were unveiled by XPS. As displayed in Fig. 4d, the full scan XPS spectrum of BS-G show the predominant C1 s peak (92.06 at%) located at 283.17 eV, O1 s peak (3.30 at%) at ca. 531.17 eV, B1 s peak (2.47 at%) at 192.17 eV, and S2p peak (2.17 at%) at 167.17 eV, suggesting the successful doping of B and S dual-heteroatoms within the graphene frameworks. Fig. 4e shows the core level spectra of C1s for the BS-G with its deconvoluted four spectral peak positions, the sp²-hybridized carbon peak found at 284.40 eV responds to graphene, and the peak at 284.97 eV demonstrates the presence of C-C, C-O and C-B, the peaks at 286.15 eV is related to C-S-C bonds and the peak at 288.05 eV illustrates the presence of C-O-B and O-C=O or -COOH. Similarly, three peaks centered at 190.58, 191.51 and 192.39 eV can be observed in the B1s core level spectra (Fig. 4f), which corresponds to B-C, BCO₂ or BC₂ and B-O bonds, respectively. Whereas the S2p spectrum (Fig. 4g) reveals sulfur is present either in thiophenic form (a lower energy doublets 2p_{3/2} and 2p_{1/2} at 163.76 and 165.30 eV representing to C-S-C) or in the form of sulfoxide groups (a higher energy doublets 2p_{3/2} and 2p_{1/2} at 167.88 and 169.21 eV representing to C-SO_x-C, sulfonate or sulfone) [44].



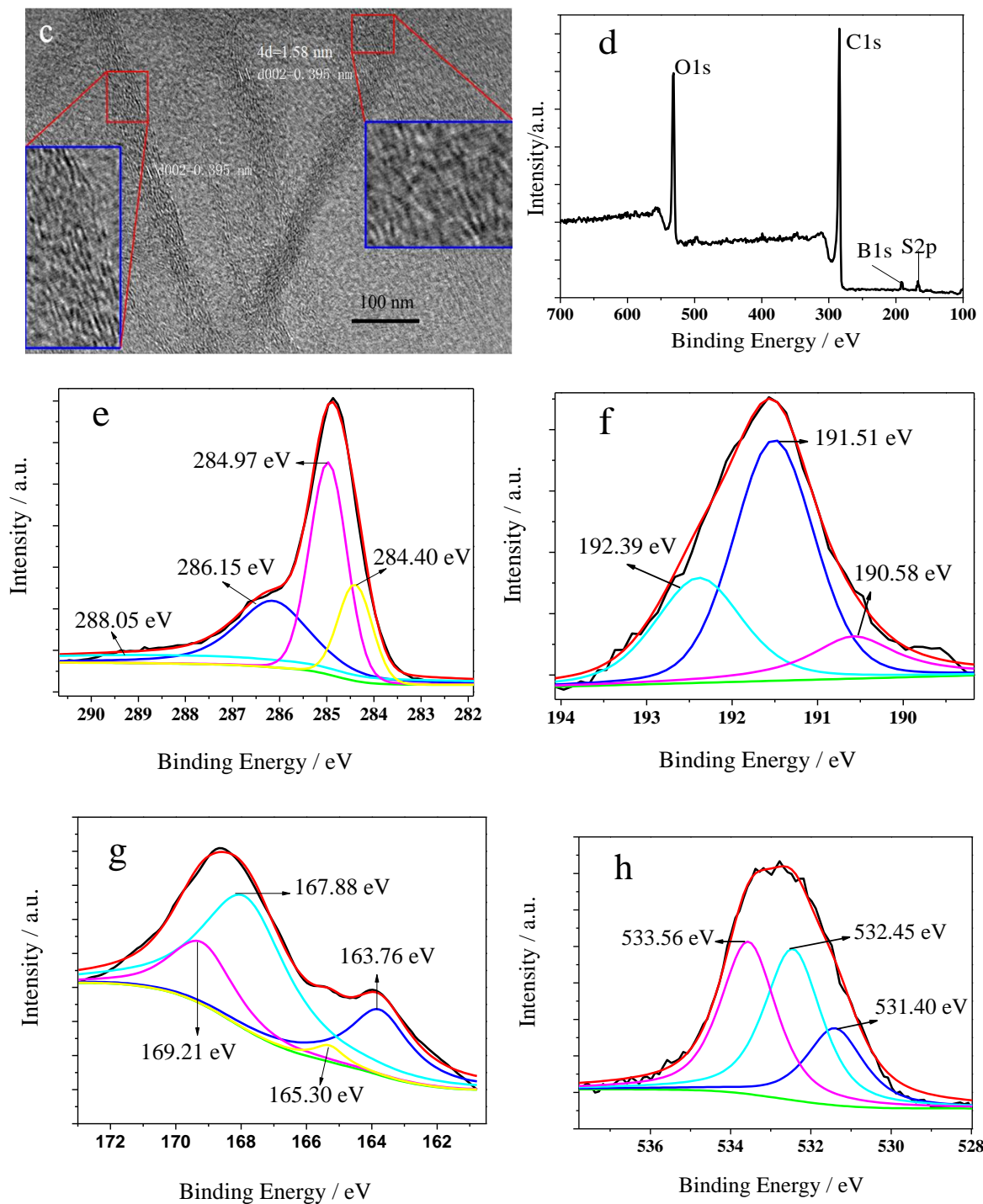


Figure 4. Morphology and structure of BS-G, (a) SEM and (b) TEM image. (c) HRTEM image of BS-G, the (002) fringe spacing was measured to be 0.395 nm ($4d=1.58$ nm). (d) XPS survey spectrum of BS-G. Deconvoluted C1s (e), B1s (f), S2p (g) and O1s (h) of XPS spectrum of BS-G.

The S element is bonded to the graphene sheets via C-SO_x-C shows that S-doping could be substituted by oxygen in the graphene nanosheets, thus the peak intensity of the C-O bond in Fig. 4e is decreased by the S-doping that could be due to the C-S bond [45]. The high-resolution O1s XPS

spectrum (Fig. 4h) shows O species correspond to HO-C=O (533.56 eV), C=O (532.45 eV) and C-OH or and C-O-C (531.40 eV). It was observed that the content of oxygen atom in the BS-G was found to 14.78 at%, suggesting that BS-G with excellent hydrophilicity and beneficial to immobilize antibodies or antigens for the successful immunosensor construction.

Both large surface area of graphene and dual-doping of B, S heteroatoms into graphene frameworks create much more defect sites are considered to strengthen dramatically the metal-support binding and benefit to anchoring of Au@Pt NRs. As the TEM images of Au@Pt NRs/BS-G hybrid nanocatalysts show in Fig. 5a, the peanut-shaped Au@Pt NRs with good dispersibility were embedded uniformly into the BS-G nanosheets without aggregation, meanwhile the transparent, and ultrathin wrinkled BS-G nanosheets can be observed. In most cases, the peanut-shaped Au@Pt NRs were singly encapsulated in BS-G nanosheets, and BS-G was tightly attached to the surface of Au@Pt NRs, which due to the produced positive charge of carbon atoms that facilitates the Au@Pt NRs adsorption [46]. Fig. 5b represents the HRTEM image of Au@Pt NRs/BS-G hybrid nanocatalysts, in which a single lattice spacing values was measured to be approximately 0.395 nm consistent with the (002) crystal faces of BS-G, corresponding well with the HRTEM images.

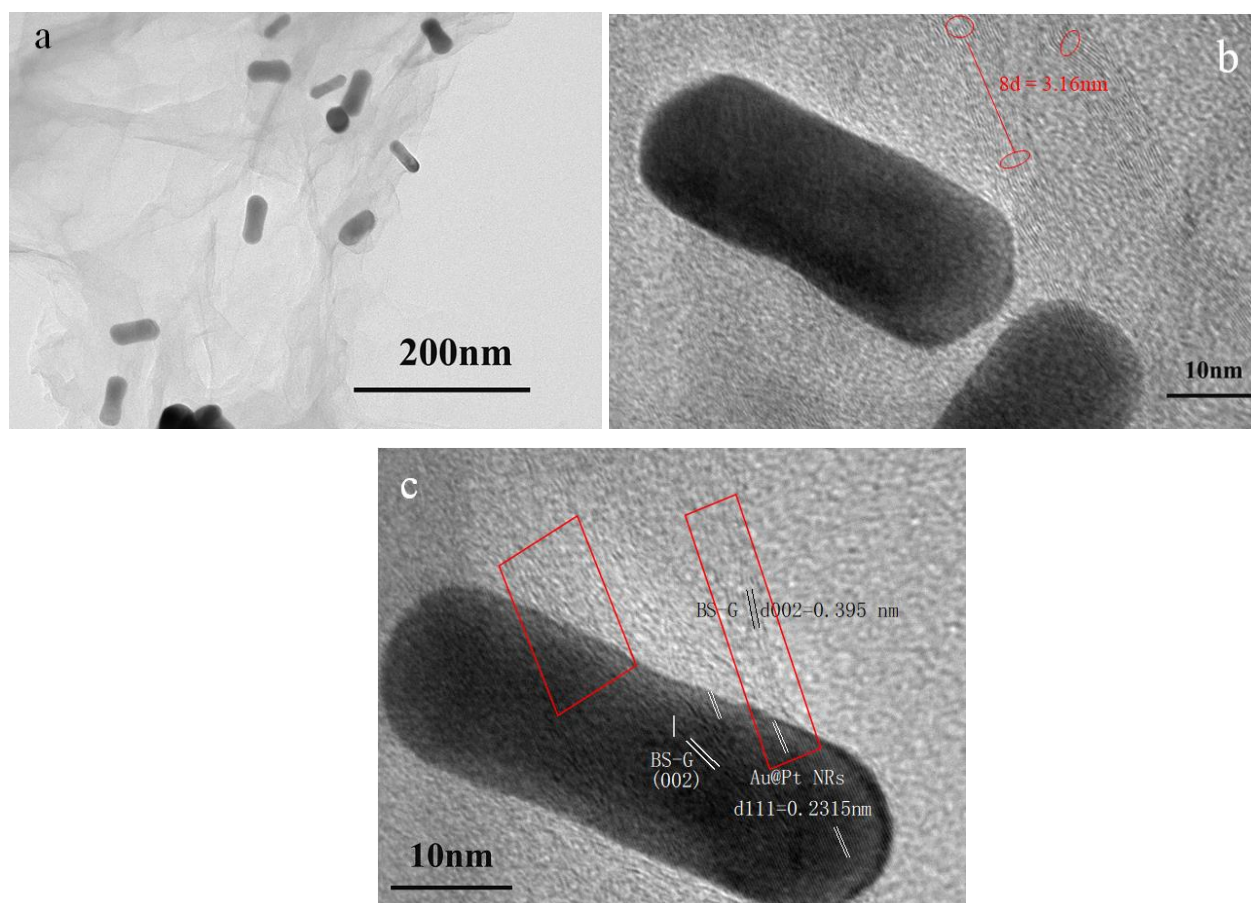


Figure 5. TEM (a) and HRTEM (b) images of the Au@Pt NRs/BS-G hybrid nanocatalysts at different magnifications. (c) HRTEM image of the Au@Pt NRs/BS-G hybrid nanocatalysts.

Even more interesting is Fig. 5c image shows that the (002) crystal faces of BS-G and (111)

planes of Au@Pt NRs parallel to each other, indicating doping sulfur and boron atoms produce a large number of nanoditches serve as the preferred sites for Au@Pt NRs anchoring. The probable reason being that B, S doping can transfer electron to Au@Pt NRs and increase its electron density due to the lower electronegativity of B atoms [23]. Both the coupling interactions between two heteroatoms and Au@Pt NRs as well as the functional groups (-COOH) of BS-G will be favorable for the adsorption and conjugation of anti-AFB₁, promoting the charge transfer between electrode and AFB₁, which are beneficial to the improved electrochemical immunosensing performances [30].

3.3. Electrochemical characterization of the hybrid nanocatalysts

The presented BS-G and Au@Pt NRs/BS-G hybrid nanocatalysts are demonstrated with CV and EIS measurements to investigate their electrochemical performance. The CVs of at bare GE (a), BS-G/GE (b) and Au@Pt NRs/BS-G/GE (c) were recorded in the mixed solution of 1.00 mM K₃[Fe(CN)₆] and 0.50 M KCl as shown in Fig. 6A. It is found that the current at the BS-G/GE (curve b) considerably higher than that at the bare GE (curve a), which is attribute to the combination of the B and S dopants resulting in the enhanced electrocatalytic activity. Notably, the peak current (I_p) of Au@Pt NRs/BS-G/GE (curve c) was the highest one, demonstrating that the synergistic effects of Au@Pt NRs/BS-G hybrid nanocatalysts on the electrode surface, while the Au@Pt NRs encapsulated in BS-G, resulting that the electron transfer within modified materials is more readily according to the comparability of both two faces at the interface, (002) plane of BS-G and (111) planes of Au@Pt NRs parallel to each other as shown in Fig. 5c. Furthermore, the Au@Pt NRs have high-efficiency electrocatalytic activity from the Pt nanoshell and the uncoated Au nanorods. Therefore, the Au@Pt NRs/BS-G hybrid nanocatalysts were used as perfect signal amplification to improve the sensitivity of immunosensor.

EIS measurements were made of both BS-G and Au@Pt NRs/BS-G hybrid nanocatalysts modified and unmodified gold electrode, and the Nyquist plots are displayed in Fig. 6B. The electron transfer resistance (R_{et}) can be calculated from the semicircle width of the Nyquist plots, the R_{et} value of the bare GE is 200.9 Ω (curve a), the R_{et} of the BS-G/GE dramatically decreases to 100.2 Ω , demonstrating that it is an excellent bifunctional electrocatalysts due to the synergistic effects between the doped B and S atoms, which result in rendering further enhanced catalytic performance. While on the Au@Pt NRs/BS-G/GE, the R_{et} value decreases significantly to 0.0 Ω (curve c), which is over 200.0 times less than that of the bare GE. The excellent electro-conductibility of Au@Pt NRs/BS-G hybrid nanocatalysts can be contributed to the synergistic effects of B and S atoms in tuning the electronic structure and the porous architecture.

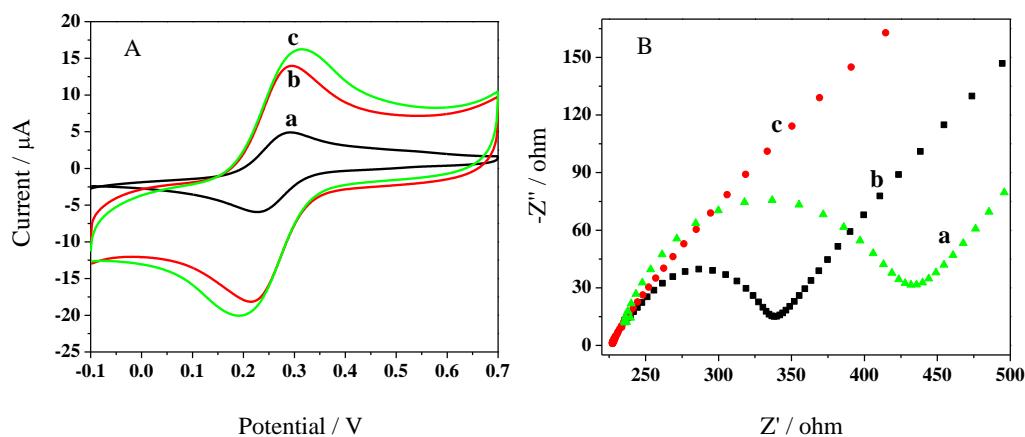


Figure 6. (A) CVs of different materials modified GE (Au@Pt NRs (b) and Au@Pt NRs/BS-G (c)) and bare GE (a) in mixed solution of 1.00 mM $\text{K}_3[\text{Fe}(\text{CN})_6]$ and 0.50 M KCl at 50.0 mV/s. (B) Nyquist diagram of different materials modified GE (Au@Pt NRs (b) and Au@Pt NRs/BS-G (c)) and bare GE (a) in mixed solution of 10.00 mM $[\text{Fe}(\text{CN})_6]^{3-/4-}$ and 0.10 M KCl (10^5 -0.1 Hz).

3.4. Electrochemical characterization of the immunosensor

CV and EIS were also employed for characterize the interfacial changes of the immunosensor during the fabrication procedure by supplying useful information on interfacial change at the electrode/electrolyte interface in Fig. 7A, B. The Au@Pt NRs/BS-G/GE (curve a) have the highest I_p and the smallest interface impedance with a diffusion limiting step. After the immobilization of anti-AFB₁ (curve b), the I_p clearly decreased and produced a small well-defined hemicycle, suggesting Au@Pt NRs/BS-G hybrid nanocatalysts have high surface areas and remarkable electron-transfer abilities. Moreover, these hybrid nanocatalysts can enhance the effective surface area of modified electrode and further facilitates the interfacial electron transfer, as a result the R_{et} is only 20.2 Ω after immobilization of anti-AFB₁. With the immobilization of BSA on the electrode surface (curve c), the current decreased gradually and the semicircular became larger (R_{et} =153.1 Ω). Afterwards, the immunosensor was incubated with AFB₁ (10.00 ng·mL⁻¹), and an apparent decrease of I_p was obtained and exhibits a significant increase of resistance (R_{et} = 318.6 Ω) (curve d). This was due presumably to the inert property of protein and the generation of antibody-antigen immunocomplexes, which prevents the diffusion ability of ferricyanide, indicating successful formation of the immobilized electrode. Moreover, owing to the special parallel crystal faces structure and accessible active area of the Au@Pt NRs/BS-G hybrid nanocatalysts, the highly oriented immobilization of AFB₁ could be modified onto the electrode.

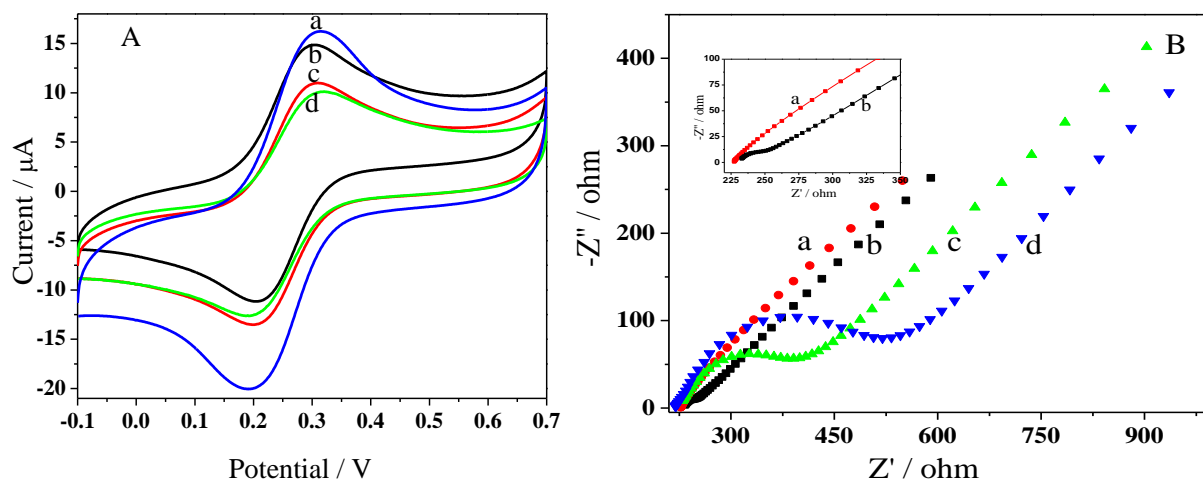
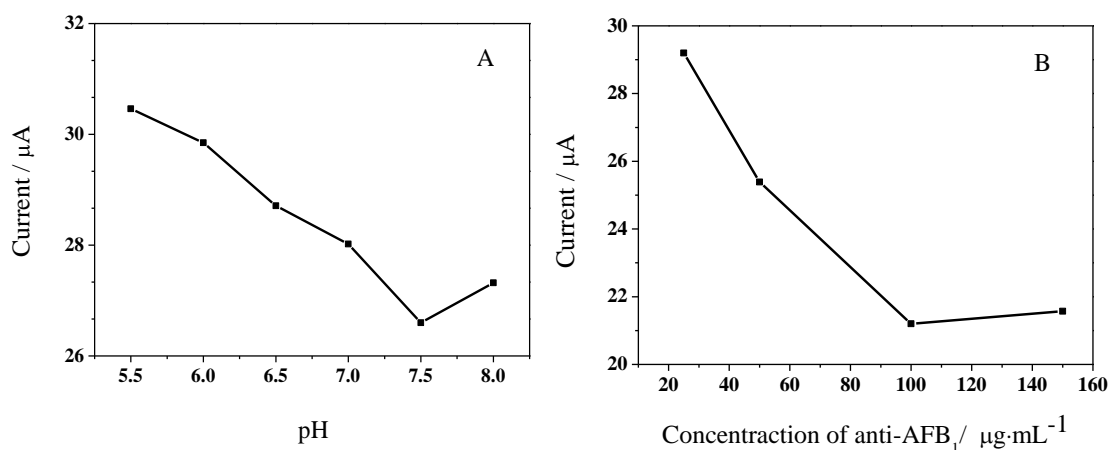


Figure 7. (A) CV profiles of Au@Pt NRs/BS-G/GE (a), anti-AFB₁/Au@Pt NRs/BS-G/GE (b), BSA/anti-AFB₁/Au@Pt NRs/BS-G/GE (c), and AFB₁/BSA/anti-AFB₁/Au@Pt NRs/BS-G/GE (d). All measurements were processed in N₂-saturated mixed solution of 1.00 mM K₃[Fe(CN)₆] and 0.50 M KCl at 50.0 mV/s. (B) Nyquist diagram of the Au@Pt NRs/BS-G/GE (a), anti-AFB₁/Au@Pt NRs/BS-G/GE (b), BSA/anti-AFB₁/Au@Pt NRs/BS-G/GE (c) and AFB₁/BSA/anti-AFB₁/Au@Pt NRs/BS-G/GE (d) in mixed solution of 10.00 mM [Fe(CN)₆]^{3-/4-} and 0.10 M KCl (10⁵ to 0.1 Hz). The concentration of anti-AFB₁ and AFB₁ are 100.00 $\mu\text{g}\cdot\text{mL}^{-1}$ and 10.00 $\text{ng}\cdot\text{mL}^{-1}$, respectively.

3.5. Determination of optimized conditions for immunoassay of AFB₁

To obtain excellent performance of the immunosensor, the experimental conditions about the pH of PBS, the concentration of anti-AFB₁, the immobilization time of anti-AFB₁, and the incubation time between antibody and antigen were optimized by recording DPV (Fig. 8). The pH of PBS may affect the activity of anti-AFB₁ and AFB₁, it was found that the current decreased with the increasing of pH value at the beginning, and reaching minimum value at pH 7.5, then increased steeply at pH 8.0 due to the result of protein denaturation. A stable immuno-complex was generated between anti-AFB₁ and AFB₁ at pH 7.5, which was selected as the supporting electrolyte for the current detections (Fig. 8A).



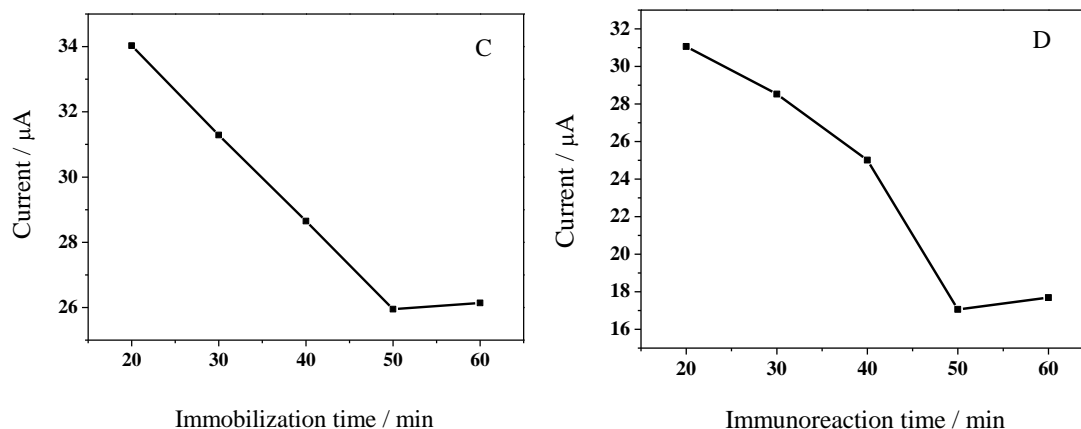


Figure 8. (A) Effect of pH of PBS on I_p of the proposed immunosensor. (B) Effect of anti-AFB₁ concentration on I_p of the immunosensor. (C) Effect of anti-AFB₁ immobilization time on I_p of the immunosensor. (D) Effect of AFB₁ immunoreaction time on I_p of the immunosensor. The experimental conditions were optimized by recording DPV toward mixed solution of 10.00 ng·mL⁻¹ AFB₁ (0.10 M PBS), 10.00 mM [Fe(CN)₆]^{3-/4-} and 0.10 M KCl at 50 mV/s vs. Ag/AgCl.

As shown in Fig. 8B, the I_p decreased to be a steady value when the concentration of immobilized anti-AFB₁ reached to 100.00 μg·mL⁻¹, indicated that the best concentration of anti-AFB₁ was 100.00 μg·mL⁻¹ for this immunosensor and used throughout the experiment process.

The incubation time of anti-AFB₁ is another significant factor to be optimized. In Fig. 8C, the DPV response decreased with the increasing of incubation time of anti-AFB₁ and was nearly stable over 50.0 min, indicating the saturated adsorption of anti-AFB₁ on Au@Pt NRs/BS-G/GE was reached after 50.0 min. Therefore, 50.0 min was selected as the optimized anti-AFB₁ assembly time.

Finally, the incubation time of AFB₁ would have an important influence on the immunoreaction. The DPV response signal decreased gradually with the increasing incubation time from 20.0 to 60.0 min in Fig. 8D, until it reached a plateau at 50.0 min. Thus, 50.0 min was selected as the optimal AFB₁ immobilization time.

3.6. Analytical performance of designed immunosensor

After the optimal conditions were established, the parameters were used to evaluate the performance of the electrochemical immunosensor, the DPV responses were investigated in 0.10 M PBS with varying concentration of AFB₁ (Fig. 9A). The I_p of the immunosensor showed a linearly decrease with successive augment AFB₁ concentrations ranging from 0.00 to 60.00 ng·mL⁻¹. Fig. 9B indicated a linear relationship between the I_p values with AFB₁ concentration was found in AFB₁ concentration range of 0.025~60.00 ng·mL⁻¹. The linear equation was I_p = 35.494 - 0.470c, with a statistically significant correlation coefficient of 0.995. The calculated detection limit of 0.0052 ng·mL⁻¹ (S/N=3) was estimated, much lower than that obtained on the GC/CRGO/SPE biosensor [47], the BSA/anti-AFB₁/AuNPs/PEDOT-GO/GCE [48] and the BSA/anti-AFB₁/AuNPs/PEDOT/ITO [49]. The low detection limit of this electrochemical immunosensor can be attributed to Au@Pt NRs/BS-G hybrid

nanocatalysts with numerous remarkable properties, which could improve the sensitivity of immunosensor.

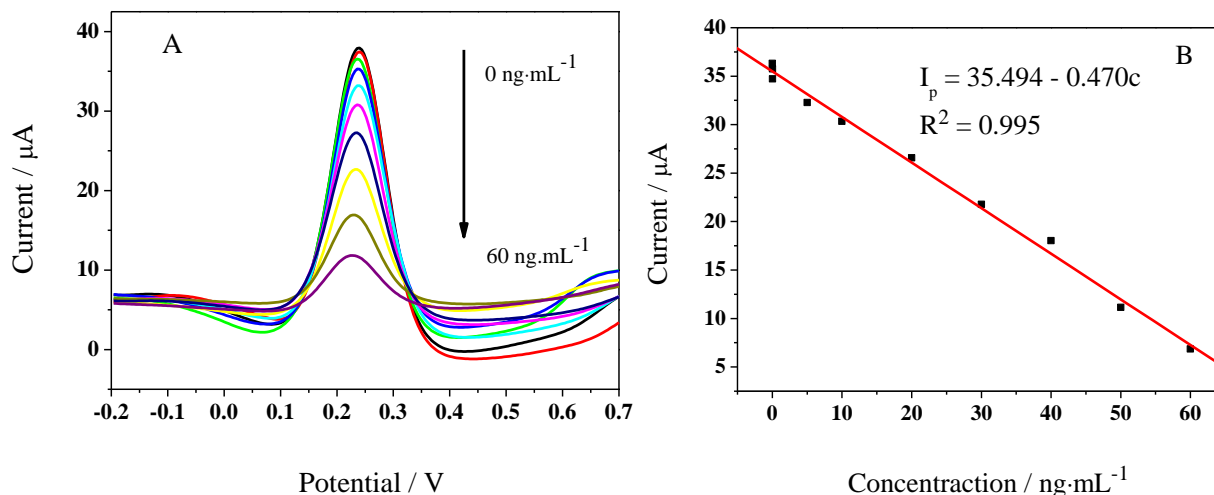


Figure 9. (A) DPV responses to AFB₁ concentrations (from top to bottom: 0.00, 0.025, 0.05, 5.00, 10.00, 20.00, 30.00, 40.00, 50.00 and 60.00 ng·mL⁻¹). (B) The linear relationship of the I_p of the immunosensor with AFB₁ concentration.

3.7. Nonspecific interactions and the reproducibility and stability

To study the specificity of the designed immunosensor, two potential interfering mycotoxins of Aflatoxin M₁ (AFM₁) and Aflatoxin B₂ (AFB₂) were tested by recording DPV with the concentrations twice as that as 40.00 ng·mL⁻¹ AFB₁ (Fig. 10). Using the current response of without AFB₁ as a reference, the DPV response decreased gradually immunoreactions with AFB₁, but alone with no obvious response change to AFB₂ and AFM₁, and the cross reactivity were calculated to be 3.98% and 15.55%, respectively. The relatively high cross reactivity of AFM₁ stem from AFM₁ is the metabolite of AFB₁. This result indicates that the designed immunosensor possessed excellent specificity.

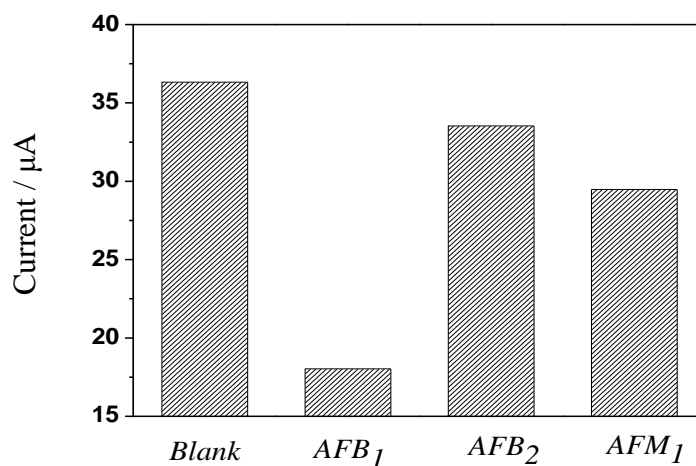


Figure 10. The specificity of the proposed immunosensor for AFB₁ detection

Five reduplicative measurements of AFB₁ at 0.50 ng·mL⁻¹ and 40.00 ng·mL⁻¹ were investigated to evaluate the reproducibility of immunosensor. The relative standard deviations (RSD) of the I_p were 5.83% and 4.75%, respectively, demonstrating an acceptable reproducibility and precision of the proposed immunosensor for AFB₁ detection.

Additionally, stability is important for immunosensor, the modified immunosensor was kept in a refrigerator at 4.0 °C. It was found that 97.6% and 92.5% of the initial response of the immunosensor could be determined after 7.0 days and 20.0 days of repeated measurements, respectively. The results indicating the immunosensor possessed good long-term stability.

3.8. Sample analysis

Table 1. Results of AFB₁ detection in spiked rice and peanut samples (n=3).

Sample	Added (ng·mL ⁻¹)	Found (ng·mL ⁻¹)	Recovery (%)	RSD (%)
Rice	30.00	31.9	103.6	1.80
	15.00	15.4	100.8	1.42
Peanuts	30.00	34.6	104.1	0.29
	15.00	15.8	101.2	0.68

The feasibility of our proposed method to evaluate AFB₁ levels in a complex matrix was also monitored by the standard addition method. Initially, we spiked AFB₁ standards (30.00 ng·mL⁻¹ and 15.00 ng·mL⁻¹) into blank rice and peanut homogenate, followed by a centrifugation procedure and extracted by methanol-water. The rice and peanut samples were determined by DPV, the recovery was in the range of 103.6%~104.1% and the RSD were 1.80% and 0.29% (Table 1), demonstrated that the designed immunosensor can be applied more reliably and effectively in AFB₁ detection.

4. CONCLUSIONS

In summary, a novel, multifunctional and ultraefficient electron-transfer abilities hybrid nanocatalyst been developed to serve as a signal amplifier to the design of immunosensing for determination of AFB₁. Firstly, the incorporation of B and S atoms into graphene with unique three dimension porous frameworks was achieved by microwave-assisted hydrothermal approach. Secondly, in the resulting BS-G encapsulated peanut-shaped Au@Pt NRs, ultrathin BS-G effectively enwrapped most of the individual Au@Pt NRs with excellent dispersibility. Interestingly, the two faces at the interface between (002) crystal faces of BS-G and (111) planes of Au@Pt NRs are compatible, accelerating the charge transfer between the Au@Pt NRs/BS-G hybrid nanocatalysts and AFB₁. Most interesting is the highly dispersed COOH groups and defect sites of BS-G as well as the Au@Pt NRs could be immobilization of anti-AFB₁ effectively. Therefore, the Au@Pt NRs/BS-G hybrid nanocatalysts as multi-component platform have been used for the immobilization of anti-AFB₁ for efficient determination of AFB₁ for preparation of BSA/anti-AFB₁/Au@Pt NRs/BS-G/GCE. This bioelectrode has been designed with extraordinary electron-transfer abilities, favorable selectivity,

long-term stability and ultralow detection limit ($0.0052 \text{ ng}\cdot\text{mL}^{-1}$ (S/N=3)) towards the detection of AFB₁. Furthermore, the immunosensor was successfully applied to selective detection of AFB₁ in rice and peanut samples and the recovery was in the range of 103.6%~104.1%, offering the potential application for a sensitive, simple and effective method for detecting mycotoxins.

ACKNOWLEDGMENTS

This work was supported by the Yunnan education department of Scientific Research Foundation (2018JS478, 2019J1183), Yunnan Local Colleges Applied Basic Research Projects (2018FH001-114, 2018FH001-049), the National Natural Science Foundation of China (21665008, 51362012 and 51662007), the Youth project of Yunnan Province (2014FD054), the training program of Young academic and technical talent reserve in Yunnan province (2018HB005), and Innovative Research Team (in Science and Technology) in University of Yunnan Province.

References

1. S. Sun, R. Zhao, Y. L. Xie, Y. Liu, *Food Control*, 100 (2019) 183-188.
2. T. S. Wu, Y. C. Cheng, P. J. Chen, Y. T. Huang, F. Y. Yu, B. H. Liu, *Chemosphere*, 217 (2019) 905-913.
3. L. M. Wang, F. W. Zhu, M. Chen, Y. Q. Zhu, J. B. Xiao, H. Yang, X. Q. Chen, *Food Chem.*, 271 (2019) 581-587.
4. G. Mahuku, H. S. Nzioki, C. Mutegi, F. Kanampiu, C. Narrod, D. Makumbi, *Food Control*, 96 (2019) 219-226.
5. R. J. Mo, L. He, X. M. Yan, T. T. Su, C. X. Zhou, Z. Wang, P. Z. Hong, S. L. Sun, C. Y. Li, *Electrochem. Commun.*, 95 (2018) 9-13.
6. I. Var, B. Kabak, F. Gök, Survey of aflatoxin B1 in helva, *Food Control*, 18 (2007) 59-62.
7. A. L. Manizan, M. Oplatowska-Stachowiak, I. Piro-Metayer, K. Campbell, R. Nevry, C. Elliott, D. Akaki, D. Montet, C. Brabet, *Food Control*, 87 (2018) 22-30.
8. S. Stefanovic, D. Spiric, R. Petronijevic, J. N. Trailovic, D. Milicevic, D. Nikolic, S. Jankovic, *Procedia Food Sci.*, 5 (2015) 270-273.
9. F. Y. Zhang, B. Liu, Y. Zhang, J. P. Wang, Y. Lu, J. Deng, S. Wang, *Anal. Chim. Acta*, 1047 (2019) 139-149.
10. A. Beheshti-Marnani, A. Hatefi-Mehrjardi, Z. Es'haghi, *Colloids Surf., B*, 175 (2019) 98-105.
11. P. F. Pang, Z. M. Yang, S. X. Xiao, J. L. Xie, Y. L. Zhang, Y. T. Gao, *J. Electroanal. Chem.*, 727 (2014) 27-33.
12. S. Gupta, A. Tiwari, U. Jain, N. Chauhan, *Mater. Sci. Eng., C*, 103 (2019) 109733.
13. L. Farzin, S. Sadjadi, M. Shamsipur, S. Sheibani, M. H. Mousazadeh, *Mater. Sci. Eng., C*, 97 (2019) 679-687.
14. X. L. Li, L. X. Cao, Y. J. Zhang, P. S. Yan, D. W. Kirk, *Electrochim. Acta*, 247 (2017) 1052-1059.
15. A. Sharma, A. Kumar, R. Khan, *Mater. Sci. Eng., C*, 76 (2017) 802-809.
16. Y. Xiong, K. Pei, Y. Q. Wu, H. Duan, W. H. Lai, Y. H. Xiong, *Sens. Actuators, B*, 267 (2018) 320-327.
17. P. P. Chen, X. X. Hua, J. H. Liu, H. B. Liu, F. Q. Xia, D. Tian, C. L. Zhou, *Anal. Biochem.*, 574 (2019) 23-30.
18. C. Xu, D. R. Yang, L. Mei, Q. H. Li, H. Z. Zhu, T. H. Wang, *ACS Appl. Mater. Interfaces*, 5 (2013) 12911-12920.
19. V. Sharma, N. Sinha, S. Dutt, M. Chawla, P. F. Siril, *J. Colloid Interface Sci.*, 463 (2016) 180-187.
20. Y. Lu, J. Y. Yuan, F. Polzer, M. Drechsler, J. Preussner, *ACS Nano*, 4 (2010) 7078-7086.

21. H. Q. Pan, S. Low, N. Weerasuriya, Y. S. Shon, *ACS Appl. Mater. Interfaces*, 7 (2015) 3406-3413.
22. J. Guo, T. Y. Ning, Y. S. Han, Y. Q. Sheng, C. H. Li, X. F. Zhao, Z. Y. Lu, B. Y. Man, Y. Jiao, S. Z. Jiang, *Appl. Surf. Sci.*, 433 (2018) 45-50.
23. Y. R. Sun, C. Y. Dua, G. K. Han, Y. T. Qu, L. Du, Y. J. Wang, G. Y. Chen, Y. Z. Gao, G. P. Yin, *Electrochim. Acta*, 212 (2016) 313-321.
24. M. Y. Wang, Y. Huang, X. F. Chen, K. Wang, H. W. Wu, N. Zhang, H. T. Fu, *J. Alloys Compd.*, 691 (2017) 407-415.
25. L. Shabnam, S. N. Faisal, A. K. Roy, E. Haque, A. I. Minett, V. G. Gomes, *Food Chem.*, 221 (2017) 751-759.
26. M. Shumba, T. Nyokong, *Electrochim. Acta*, 236 (2017) 212-220.
27. A. Hoggard, L.nY. Wang, L. L. Ma, Y. Fang, G. You, J. Olson, Z. Liu, W. S. Chang, P. M. Ajayan, S. Link, *ACS Nano*, 7 (2013) 11209-11217.
28. H. N. Yang, W. J. Kim, *Electrochim. Acta*, 209 (2016) 430-439.
29. Y. B. Tang, L. C. Yin, Y. Yang, X. H. Bo, Y. L. Cao, H. E. Wang, W. J. Zhang, I. Bello, S. T. Lee, H. M. Cheng, C. S. Lee, *ACS Nano*, 6 (2012) 1970-1978.
30. G. Q. Chen, Y. X. Liu, Y. Liu, Y. Tian, X. Zhang, *J. Electroanal. Chem.*, 738 (2015) 100-107.
31. I. Novodchuk, M. Irannejad, B. Wales, K. Ibrahim, J. Sanderson, M. Bajcsy, M. Yavuz, *Mater. Res. Bull.*, 111 (2019) 80-86.
32. L. Wang, X. Y. Zhang, F. Yan, H. L. W. Chan, F. Ding, *Carbon*, 98 (2016) 633-637.
33. M. L. Zhang, H. C. Tao, Y. C. Liu, C. Yan, S. Hong, J. Masa, A. W. Robertson, S. Z. Liu, J. S. Qiu, Z. Y. Sun, *ACS Sustainable Chem. Eng.*, 7 (2019) 3434-3442.
34. K. G. N. Thilawala, J. K. Kim, J. M. Lee, *J. Alloys Compd.*, 773 (2019) 1009-1017.
35. Q. Z. Chen, H. M. Liu, R. L. Zhu, X. Wang, S. Y. Wang, J. X. Zhu, H. P. He, *Microporous Mesoporous Mater.*, 225 (2016) 137-143.
36. Y. L. Qi, Y. Cao, X. T. Meng, J. Cao, X. W. Li, Q. L. Hao, W. Lei, Q. H. Li, J. Li, W. M. Si, *Sens. Actuators, B*, 279 (2019) 170-176.
37. C. Aydin, *J. Alloys Compd.*, 771 (2019) 964-972.
38. H. P. Yu, Y. J. Zhu, B. Q. Lu, *Ceram. Int.*, 44 (2018) 12352-12356.
39. B. Nikoobakht, M. A. El-Sayed, *Chem. Mater.*, 15 (2003) 1957-1962.
40. S. B. Zhang, Y. M. Shen, G. Y. Shen, S. Wang, G. L. Shen, R. Q. Yu, *Anal. Biochem.*, 494 (2016) 10-15.
41. X. Ma, M. C. Wang, J. Y. Feng, X. J. Zhao, *J. Alloys Compd.*, 637 (2015) 36-43.
42. J. F. Huang, Y. H. Zhu, C. X. Liu, Z. Shi, A. Fratalocchi, Y. Han, *Nano Lett.*, 16 (1) (2016) 617-623.
43. Z. A. Zhang, X. D. Shi, X. Yang, Y. Fu, K. Zhang, Y. Q. Lai, J. Li, *ACS Appl. Mater. Interfaces*, 8 (2016) 13849-13856.
44. M. Shumba, S. Centane, F. Chindeka, T. Nyokong, *J. Electroanal. Chem.*, 791 (2017) 36-48.
45. M. A. Baghchesara, H. R. Azimib, A. G. Shiravizadehc, M. A. M. Teridid, R. Yousefi, *Appl. Surf. Sci.*, 466 (2019) 401-410.
46. J. L. Zhu, G. Q. He, Z. Q. Tian, L. Z. Liang, P. K. Shen, *Electrochim. Acta*, 194 (2016) 276-282.
47. C. H. D. Nieto, A. M. Granero, D. Garcia, A. Nesci, G. Barros, M. A. Zon, H. Fernández, *Talanta*, 194 (2019) 253-258.
48. A. Sharma, A. Kumar, R. Khan, *Synth. Met.*, 235 (2018) 136-144.
49. A. Sharma, A. Kumar, R. Khan, *Mater. Sci. Eng., C*, 76 (2017) 802-809.